JOURNAL OF SPACECRAFT AND ROCKETS
Vol. 42, No. 4, July–August 2005

Debonding Failure of Sandwich-Composite Cryogenic Fuel Tank with Internal Core Pressure

Edward H. Glaessgen,* James R. Reeder,† David W. Sleight,* John T. Wang,* Ivatury S. Raju,‡ and Charles E. Harris§
NASA Langley Research Center, Hampton, Virginia 23681

A summary of the failure analyses and testing that were conducted to determine the cause of the X-33 liquid-hydrogen tank failure is presented. Ply-level stress analyses were conducted to explain the formation of microcracks in the plies of the inner and outer facesheet laminates of the honeycomb sandwich walls of the tank under known thermal and mechanical loads. The microcracks allowed the ingression of liquid- and gaseous-hydrogen and gaseous-nitrogen purge gas that produced higher than expected sandwich core pressures in the tank. Single cantilever beam tests were used to determine the toughness of the interface between the facesheets and honeycomb core. Fracture mechanics analyses were developed to determine strain-energy release rates for known foreign object debris shapes and sizes and known and statistically possible core internal pressures. The fracture mechanics analyses were validated by comparing with results of blowoff tests that were fabricated from undamaged tank sandwich material. Strain-energy release rates from the validated analyses were then compared with known and statistically possible values of toughness determined from the single cantilever beam tests. These analyses and tests were then used to substantiate a scenario for failure of the X-33 liquid-hydrogen tank that includes microcracking of the inner facesheets and ensuing ingression of hydrogen and nitrogen, a low bondline strength and toughness, and the presence of foreign object debris.

Nomenclature

$\bar{A}^{-1}_{jk}$	=	inverse of the laminate stiffness matrix transformed to the local coordinates
a, b	=	dimensions of debond
E_{ii}	=	elastic modulus in the ith principal material direction
$\bar{F}_x, \bar{F}_y$	=	integrated (net) forces in the x and y directions, respectively
$F_{x_i}, F_{y_i}, F_{z_i}$	=	nodal forces in the x, y, and z directions, respectively
G_{cr}	=	fracture toughness
$G_{\mathrm{I}}, G_{\mathrm{II}}, G_{\mathrm{III}}$	=	strain energy release rates in modes I, II, and III, respectively
G_{ij}	=	shear modulus in the ij principal material plane
N_x, N_y	=	individual nodal forces in the x and y directions, respectively
P_c	=	critical load
p	=	sandwich core internal pressure
Q_{ij}	=	lamina reduced stiffness
$\bar{Q}_{km}$	=	lamina transformed reduced stiffness
T	=	laminate temperature
T_0	=	stress-free temperature (assumed to be 160°C)
t	=	thickness of ply
u, v, w	=	displacements in the x, y, and z directions, respectively
u_p, v_p, w_p	=	nodal displacements in the x, y, and z directions, respectively
u_0, v_0	=	uniform displacements in the x and y directions, respectively
α_j	=	lamina coefficients of thermal expansion
α^L_j	=	coefficients of thermal expansion of the symmetric laminate
$\bar{\alpha}^l_m$	=	lamina coefficients of thermal expansion in local coordinates
$\Delta, b_{\mathrm{eq}}, b_J$	=	mesh parameters used in virtual crack closure technique calculation
δ	=	crack opening displacement
ε_j	=	lamina strains
ν_{ij}	=	Poisson's ratios
σ^M_i	=	lamina mechanical stresses
σ^T_i	=	lamina thermal residual stresses

Introduction

COMPOSITE sandwich construction has received renewed attention as a lightweight material form for aircraft and spacecraft structures because of its high stiffness-to-weight and strength-to-weight ratios. Composite sandwich structures can be more cost effective to manufacture than traditional skin-stringer structures and can have better fatigue resistance.[1] Additionally, recent studies have determined that sandwich construction has the potential to be the lightest and lowest-cost manufacturing concept for aerospace vehicle fuselage structures.[1] Sandwich structures can be constructed of a metallic or nonmetallic core bonded between metallic or fiber-reinforced composite facesheets. Such composite sandwich structures consisting of aramid phenolic core and carbon/epoxy facesheets have shown considerable promise for use in aerospace applications; however, implementation of such technology is not without difficulty and risk. A manifestation of such difficulty and risk arose in conjunction with the X-33 program.

The liquid hydrogen (LH_2) tank that was developed for the X-33 vehicle (see Fig. 1) experienced an unexpected failure during protoflight testing at NASA Marshall Space Flight Center on 3 November 1999. The following is an excerpt from the final report[2] by the investigation team that describes the tank and the failure scenario:

> The tank was a conformal, load-bearing, composite sandwich structure, consisting of four lobes that provided packaging efficiency for integration into the vehicle. Protoflight testing under

Received 2 October 2003; revision received 27 May 2004; accepted for publication 27 May 2004.

*Aerospace Engineer, Analytical and Computational Methods Branch, MS 240. Senior Member AIAA.

†Materials Research Engineer, Mechanics and Durability Branch, MS 188E.

‡Structures Discipline Chief Engineer, NASA Engineering and Safety Center, MS 112. Fellow AIAA.

§Principal Engineer, NASA Engineering and Safety Center, MS 112.

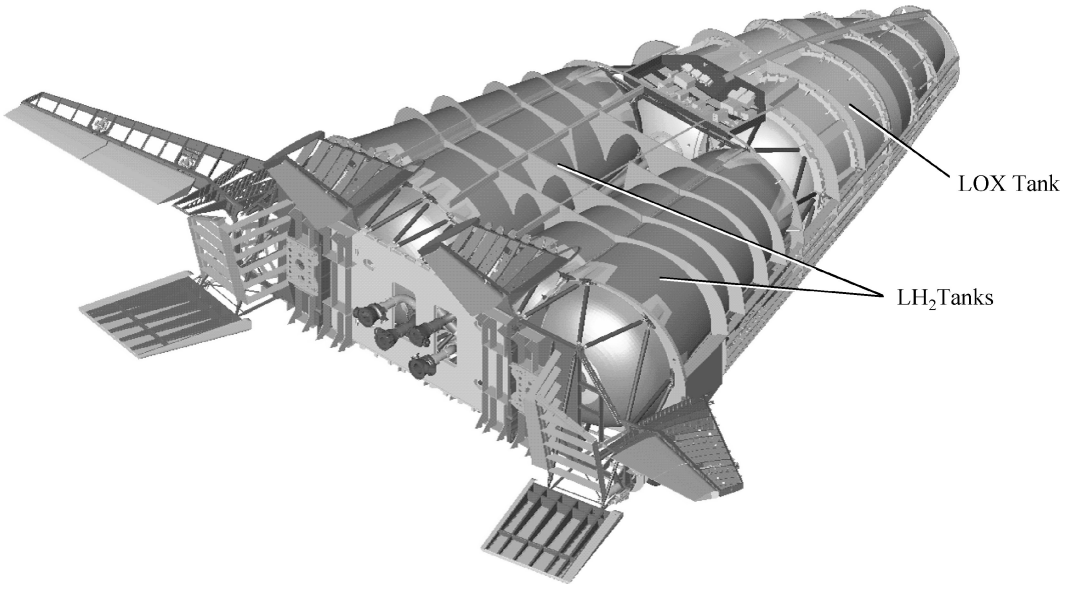

Fig. 1 X-33 vehicle.[2]

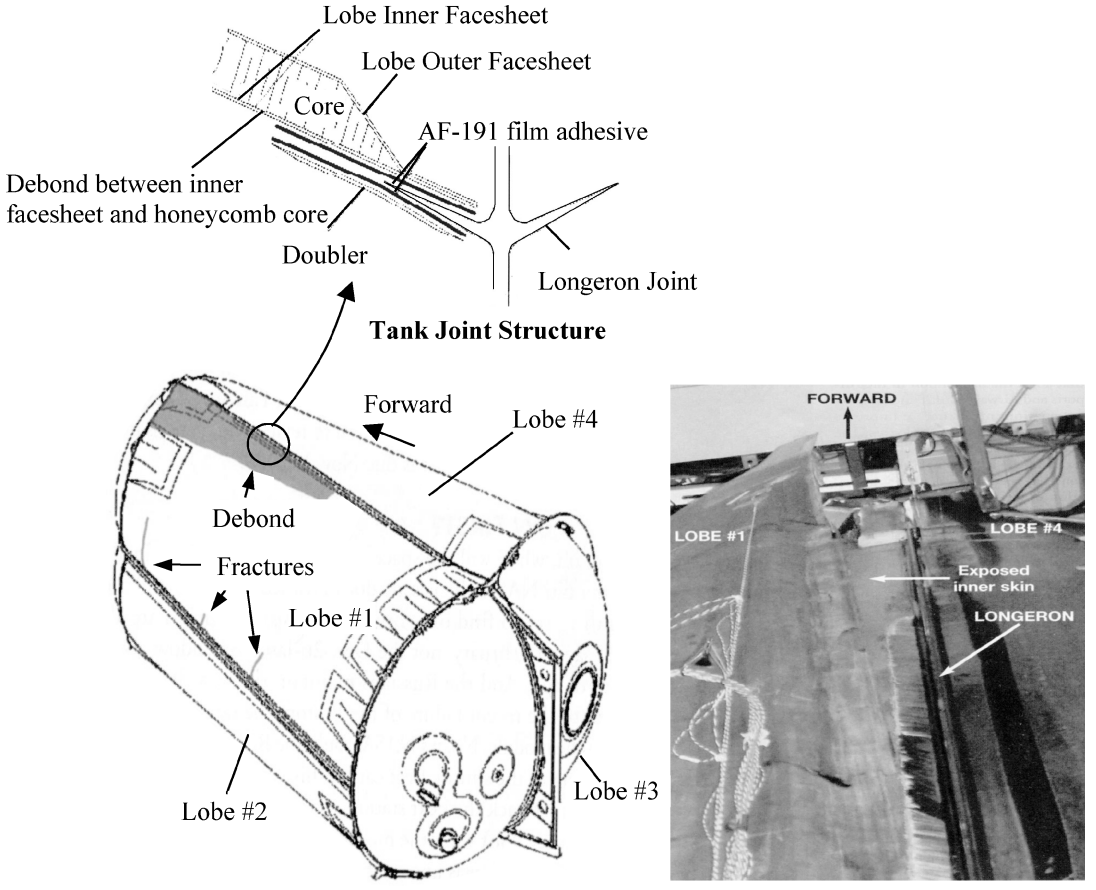

a) LH_2 tank failure location **b) Photograph of local failure region**

Fig. 2 X-33 composite liquid-hydrogen tank failure.[2]

cryogenic conditions to −253°C and to expected flight loads was necessary to clear the tank for use in the X-33 vehicle. After successful completion of the first protoflight pressure and loads test, the tank was drained of its LH_2, and a purge of the tank began. Approximately 15 minutes after the tank was drained, the outer facesheet and core of Lobe #1 separated from the inner facesheet.

Figure 2 shows the X-33 composite LH_2 tank after the failure, with Fig. 2a showing the extent of the debond in lobe 1 near one of the tank joints. The inset to Fig. 2a shows details of the local tank construction and the location of the debond between the inner facesheet and honeycomb core. Also shown in Fig. 2a are several fractures on the opposite side of the lobe that are believed to have occurred after the debond event. A photograph of the local debonded (exposed) region near the longeron is shown in Fig. 2b.

A team from NASA, the tank manufacturer, and several independent consultants investigated the incident during a three-month period from mid-November 1999 to early February 2000. The team

followed a classic fault tree approach[3] with a combination of analyses, tests, and data evaluations to determine potential causes of the failure. The most probable cause of the failure was determined to be a combination of the following phenomena: 1) microcracking of the inner facesheet with subsequent infiltration of liquid and gaseous hydrogen; 2) cryopumping of the exterior nitrogen purge gas; 3) higher than expected core pressures resulting from the liquid-hydrogen, gaseous-hydrogen, and gaseous-nitrogen purge gas; 4) reduced bondline strength and toughness; and 5) manufacturing flaws and defects.

The objective of this paper is to present the microcrack and fracture mechanics analyses and associated tests that were conducted during the process of the investigation of the X-33 liquid-hydrogen tank failure. In this paper, the analyses used to predict the microcracking in the inner and outer facesheet laminates under thermal and mechanical loads, the analyses used to predict the debonding of the composite sandwich structure under internal pressure loads, and the tests used to determine bondline toughness and verify the fracture mechanics analyses are discussed. The effects of thermal and mechanical loading on facesheet stresses as well as the effects of debond size and shape, material properties, and magnitude of the pressure loading on strain-energy release rates are considered. Computed strain-energy release rates are compared with experimentally determined values to validate the fracture mechanics analyses and determine the conditions required for debond growth.

X-33 Composite Tank

The X-33 LH_2 composite tank is a multilobe graphite/epoxy tank with three major subcomponents: the aft dome/bulkhead, the barrel section including the lobe skin assembly, and the forward dome/bulkhead. Figure 3a shows details of the LH_2 tank assembly including the IM7/977-2 carbon/epoxy facesheets and honeycomb Korex core, Fig. 3b shows the overall dimensions of the tank, and Fig. 3c shows a photograph of the LH_2 tank during construction. The honeycomb composite sandwich structure of the LH_2 tank consisted of an outer facesheet, honeycomb core and inner facesheet as shown in Fig. 4. Configurational details of the LH_2 tank are given in Table 1. Nominal toughness for the AF-191 adhesive used to join

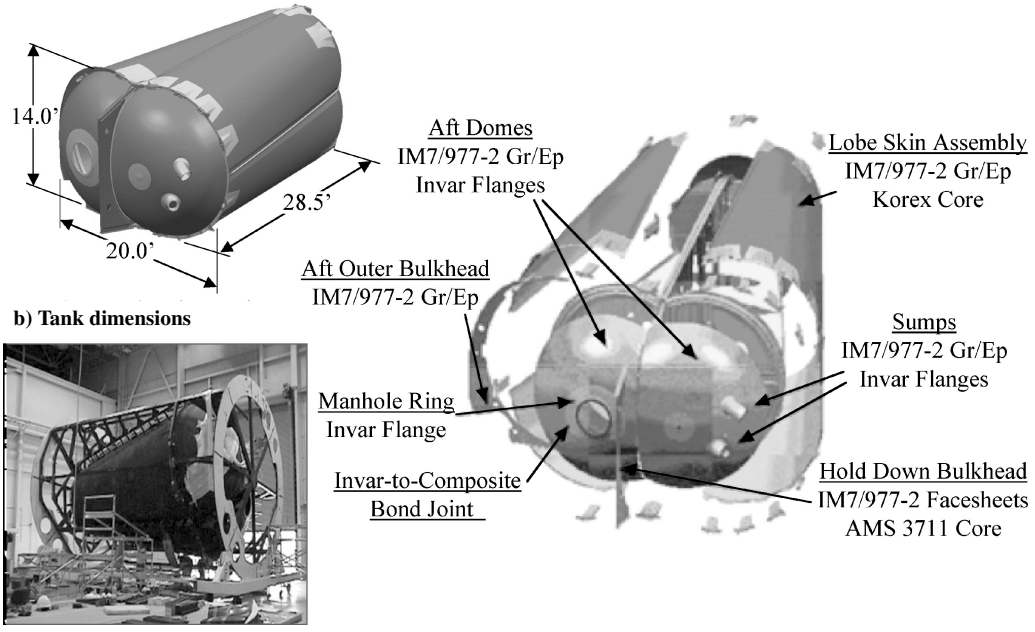

Fig. 3 X-33 liquid-hydrogen composite tank assembly.[2]

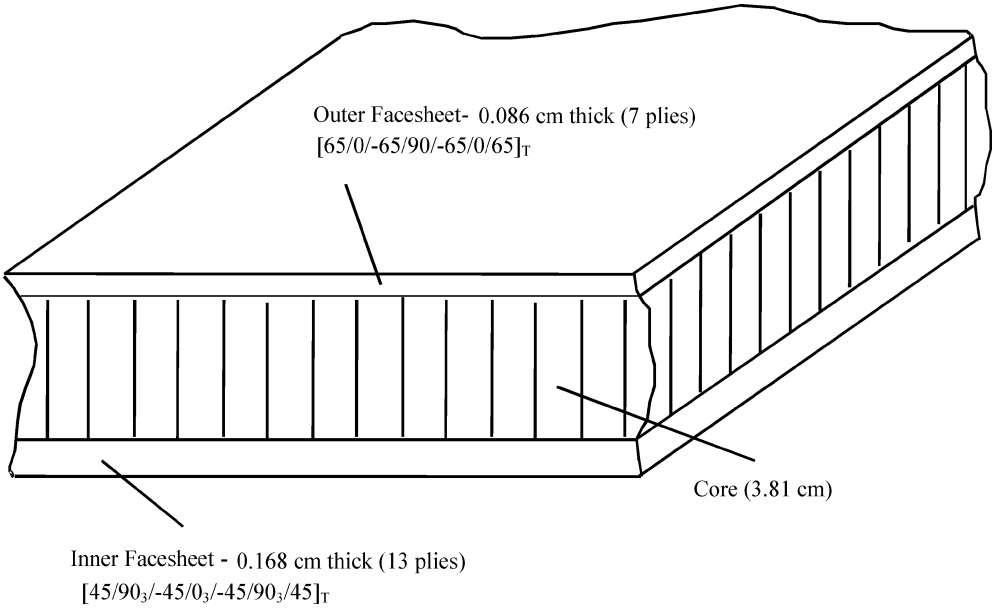

Fig. 4 Configuration of honeycomb sandwich structure.

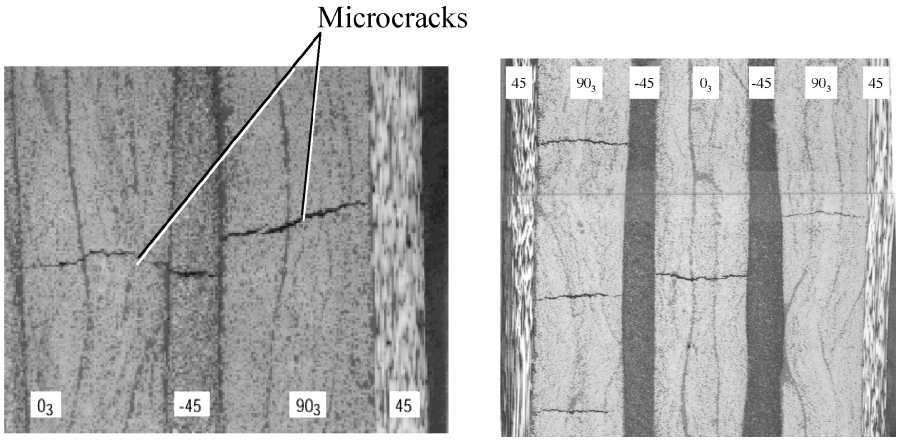

a) Inner facesheet microcracking (sectioned at 45 deg)

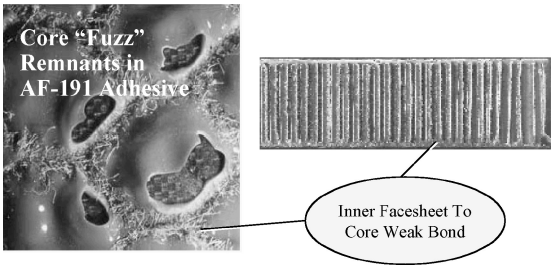

b) Weak core-facesheet bond

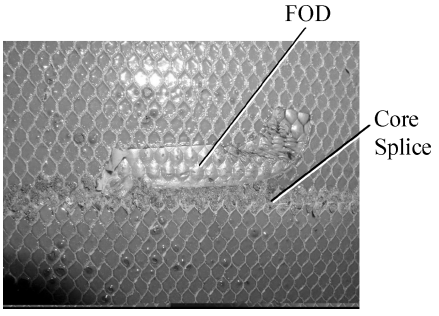

c) Foreign object debris (Teflon tape) in core

Fig. 5 Contributors to the X-33 composite liquid-hydrogen tank failure.[2]

Table 1 LH_2 tank material configuration

Component	Plies	Material	Stacking sequence	Thickness, cm
Inner facesheet	13	IM7/977-2	[45/90$_3$/ −45/0$_3$/ −45/90$_3$/45]	0.178
Core	——	Korex 3/16-3.0	——	3.81
Outer facesheet	7	IM7/977-2	[65/0/ −65/90/ −65/0/65]	0.086

the facesheets to the core is about 1210 N · m/m^2 (Ref. 4); however, the in situ facesheet-to-core bondline toughness was much lower, as will be discussed later in this paper.

Composite-Tank Failure Scenario

The failure scenario of the composite tank from the failure investigation report[2] has been hypothesized as follows. First, the inner composite facesheet microcracked as shown in Fig. 5a under combined thermal and mechanical loads, allowing liquid- and gaseous-hydrogen ingression and cryopumping of the exterior nitrogen purge gas. The liquid hydrogen then changed phase to gaseous hydrogen as the tank was drained, and the tank temperature increased to the ambient temperature, resulting in a very high internal core pressure. Second, the bond between the honeycomb core and the carbon/epoxy facesheets was much less tough than expected as a result of poor bonding and core fuzz remnants, as shown in Fig. 5b. Third, several pieces of foreign-object debris (FOD) were found at the bondline, one of which is shown in Fig. 5c. The degraded bondline and FOD provided an initial debond that precipitated the debonding of the outer facesheet and core from the inner facesheet of the tank. The upcoming sections of this paper present the role of these contributors in the composite-tank failure.

Stress Analysis of the Inner and Outer Facesheets for Microcracking

Method of Calculating Ply-Level Stresses

Microcracking was evident in samples taken from the inner facesheet of the composite tank as shown in Fig. 5a. A ply-level stress analysis was conducted to determine whether microcracks would form in the various plies of the inner and outer facesheet laminates under known thermal and mechanical loads. Using classical lamination theory (CLT), the thermal residual stresses in the plies of a laminate caused by cool down from the stress-free temperature are given by

$$\sigma_i^T = Q_{ij}\left(\alpha_j^L - \alpha_j\right)(T - T_0), \qquad \alpha_j^L = \bar{A}_{jk}^{-1} \sum_l \bar{Q}_{km}^l \bar{\alpha}_m^l t^l \tag{1}$$

Table 2 Properties[a] used in the laminate stress analysis

Laminate	Direction	CTE measured, $\mu\varepsilon/C$ Source 1[b]	CTE measured, $\mu\varepsilon/C$ NASA	CTE by CLT, $\mu\varepsilon/C$
Inner skin	Longitudinal	3.6	3.85	3.80
	Transverse	2.3	1.64	2.34
Outer skin	Longitudinal	2.9	3.80	3.80
	Transverse	1.1	1.22	2.32

[a]Ply properties: $E_{11} = 149.6$ GPa, $E_{22} = 13.4$ GPa, $G_{12} = 8.1$ GPa, $\nu_{12} = 0.413$, $\alpha_m = 16.67\ \mu\varepsilon/C$ (selected to match inner skin measured CTEs), and $\alpha_f = 1.26\ \mu\varepsilon/C$.
[b]See Ref. 2 for additional information.

Standard CLT equations were also used to calculate the ply-level transverse (normal to the fiber direction) mechanical stresses in the tank as a result of internal pressure. The ply mechanical stresses are computed by

$$\sigma_i^M = -Q_{ij}\varepsilon_j \tag{2}$$

where ε_j is the applied strain. Local strains, determined by finite element analysis of the tank, were 0.20% in the hoop direction and 0.13% in the longitudinal direction.

The ply properties used in the CLT analysis were obtained from several sources and are given in Table 2 (Ref. 2). The coefficients of thermal expansion (CTE) were backcalculated as those required to match the CLT calculations of the CTE to the measured laminate CTEs for the inner and outer facesheet laminates (Table 2). The

Table 3 Ply-level transverse stresses in inner and outer facesheet laminates

Laminate/material system	Thermal stress, MPa	Mechanical stress, MPa	Total stress, MPa
Inner facesheet, IM7/977-2, $\Delta T = -431°C$			
90-deg plies	69.6	29.0	98.6
0-deg plies	74.5	34.5	109.0
45-deg plies	72.4	31.7	104.1
Outer facesheet, IM7/977-2, $\Delta T = -279°C$			
90-deg plies	44.1	29.0	73.1
0-deg plies	46.9	34.5	81.4
45-deg plies	44.8	29.6	74.4

Table 4 Transverse strength and modulus of IM7/977-2 from several sources

Source	90-deg tensile strength, MPa	E_{22} modulus, GPa
Source 2[a]	75.2 (RT)	7.58 (RT)
Source 2[a]	85.5 (RT)	8.27 (RT)
NASA	71.7 (RT)	9.17 (RT)
Source 1[a]	39.3 (−253°C)	13.4 (−253°C)
Source 3[a]	64.1 (−253°C)	13.8 (−253°C)

[a]See Ref. 2 for additional information.

laminate stacking sequence for the inner and outer facesheets was given in the section X-33 Composite Tank discussed earlier.

Stress Analysis Results

The calculated transverse residual stresses caused by the thermal cooldown, the transverse mechanical stresses caused by tank pressurization, and the total (combined thermal and mechanical) stresses are given in Table 3 for the inner and outer facesheet laminates. The thermal residual stresses in the inner facesheet are appreciably higher than those in the outer facesheet because the inner facesheet was significantly colder during the test (−253°C) than the outer facesheet (−101°C). The mechanical stresses caused by the tank internal pressure are approximately the same for both laminates. Measured values of transverse (90-deg) ply strength and modulus for IM7/977-2 at room temperature (RT) and −253°C are presented in Table 4.

By comparing the computed stresses in Table 3 to the transverse ply strength values in Table 4, it is observed that the stresses in the inner facesheet were large enough to promote microcracking while the stresses in the outer facesheet probably were at or below the threshold for microcracking. This comparison is usually referred to as first-ply failure and is considered to be very conservative because the transverse tensile strength measured from a 90-deg unidirectional laminate is a result of failure at the weakest location in the test specimen. Thus, these predictions suggest that extensive microcracking is likely to occur in the inner facesheet, but that microcracking is less likely to occur in the outer facesheet. This difference would allow liquid hydrogen to enter the core through the inner facesheet but not allow it to escape through the outer facesheet.

Pressures within the composite sandwich walls of the tank were measured using pressure transducers stationed at various locations. However, no pressure transducer was located at the site where the debond is believed to have initiated. Additionally, the pressure in the failed lobe (lobe 1) varied considerably depending on location with the mean, highest measured, and highest statistically possible (3σ) values of pressure determined to be approximately 257, 464, and 786 kPag, respectively. Because the local pressure at failure could not be determined, these three values of pressure (mean, highest measured, and highest statistically possible) are used in the characterization of failure within this paper.

Fracture Mechanics Analyses of Debonds in Sandwich Structure

Description of the Model and Computational Procedure

The roles of the weak core-to-facesheet bondline (Fig. 5b) and foreign-object debris (Fig. 5c) in the tank failure are explained using fracture mechanics analyses. Fracture mechanics analyses of debonds were performed assuming that there were various shape and size debonds between the core and inner facesheet. A three-dimensional finite element analysis[5] incorporating the ABAQUS[6] general-purpose finite element computer program was used to analyze the problem. The materials were assumed to be linear elastic, and the displacements were assumed to be geometrically nonlinear. In the finite element models considered here, the outer facesheet, inner facesheet, and core were idealized as homogeneous orthotropic materials. The properties used for these materials and the sources from which they were obtained are presented in Table 5. Several of these values, including bending moduli of the inner and outer facesheets and out-of-plane core moduli, were obtained by correlating two-dimensional (plane-strain) finite element models of the single-cantilever-beam specimens to data obtained from single-cantilever-beam tests (SCB) performed on the sandwich structure. The correlation of the plane strain models to experimental results is described in the Appendix.

Table 5 Material properties used in finite element models

	Inner facesheet		Outer facesheet		
Property	Extension	Bending	Extension	Bending	Core
E_{11}, GPa	48.88[a]	19.3[b]	48.13[a]	47.64[b]	0.004[c]
E_{22}, GPa	78.6[a]	77.9 [b]	76.5[a]	43.3[b]	0.004[c]
E_{33}, GPa	6.9[c]	6.9[c]	6.9[c]	6.9[c]	0.140[b]
G_{12}, GPa	14.55[a]	13.31[a]	15.44[a]	10.89[a]	0.004[c]
G_{13}, GPa	5.5[c]	5.5[c]	5.5[c]	5.5[c]	0.0745[b]
G_{23}, GPa	5.5[c]	5.5[c]	5.5[c]	5.5[c]	0.0159[b]
ν_{12}	0.156[a]	0.125[a]	0.169[a]	0.202[a]	0.25[c]
ν_{13} and ν_{23}	0.25[c]	0.25[c]	0.25[c]	0.25[c]	0.02[c]

[a]Classical lamination theory with NASA TM3102 lamina properties.
[b]Fit to single cantilever beam results.
[c]Engineering judgment.

Table 6 Debond configurations and pressures considered in the flat-panel analyses

Parameter	Value
a, cm	1.27, 2.54, 3.81
b, cm	3.81, 5.08, 7.62
p, kPa	275.8, 551.6, 827

Both flat- and curved-panel configurations were considered. First, a flat panel with exterior dimensions of 30.5 × 30.5 cm with a rectangular debond of various sizes ($a \times b$) and aspect ratios (a/b) was considered, as shown in Fig. 6a. The sandwich panel was subjected to a core pressure p that was applied to the interior nodes of the elements defining the inner and outer facesheets in the direction of the outward normal to the inner surfaces of both of the facesheets. Table 6 lists the dimensions a and b of the debond configurations that were analyzed and the pressures that were considered. Next, a curved panel with a radius of curvature of 122 cm containing a circumferential rectangular debond with b held constant at 7.62 cm and values of a and p given in Table 6 was analyzed (Fig. 6b).

The debonded sandwich panel was modeled with 20-noded quadratic hexahedron finite elements (ABAQUS C3D20) as shown in Fig. 7. The facesheets were modeled with one quadratic element through the thickness. The core was modeled with four elements of unequal z dimension through the thickness (Fig. 7) with the elements modeling the core nearest the inner facesheet having the same thickness as the elements modeling the inner facesheet. To simplify the calculation of the strain-energy release rates, the modeling was made such that the element sizes ahead of and behind the debond front were identical.

Boundary Conditions

Three sets of boundary conditions were considered in the analyses. Boundary condition Set I represents repeating unit boundary conditions about the $x = 0$ and 30.5-cm planes and the $y = 0$ and 30.5-cm planes. Boundary condition set II represents repeating

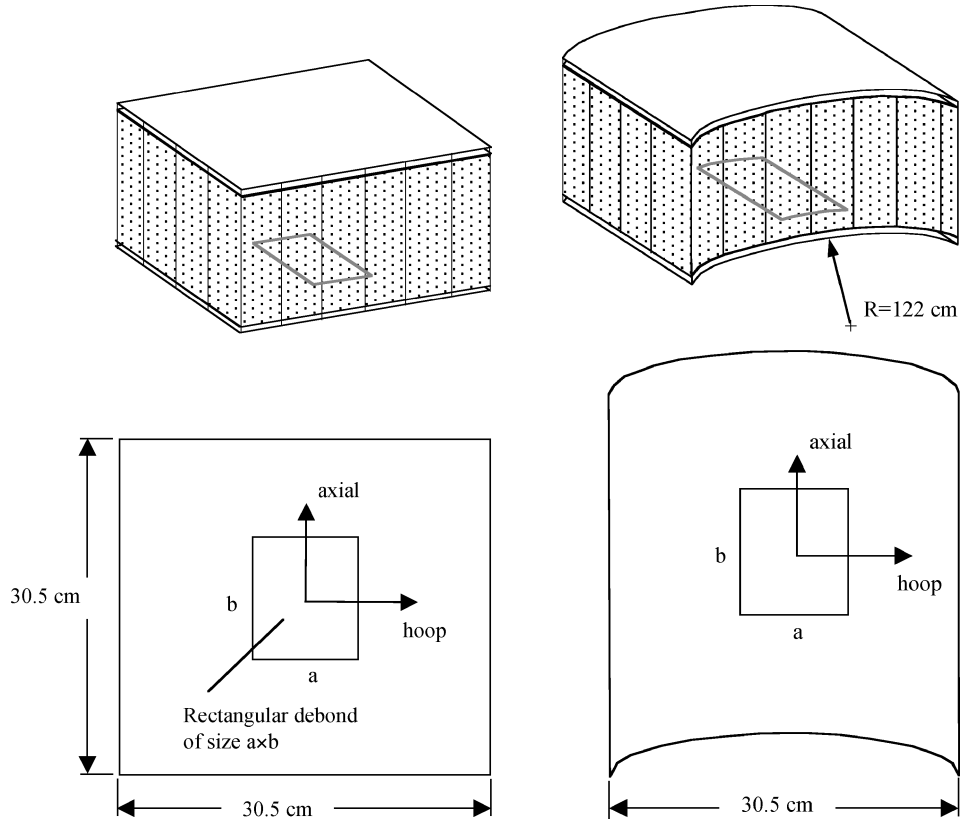

a) Rectangular debond in a flat honeycomb sandwich plate

b) Rectangular debond in a curved honeycomb sandwich plate with 122-cm radius of curvature

Fig. 6 Flat and curved debond configurations considered.

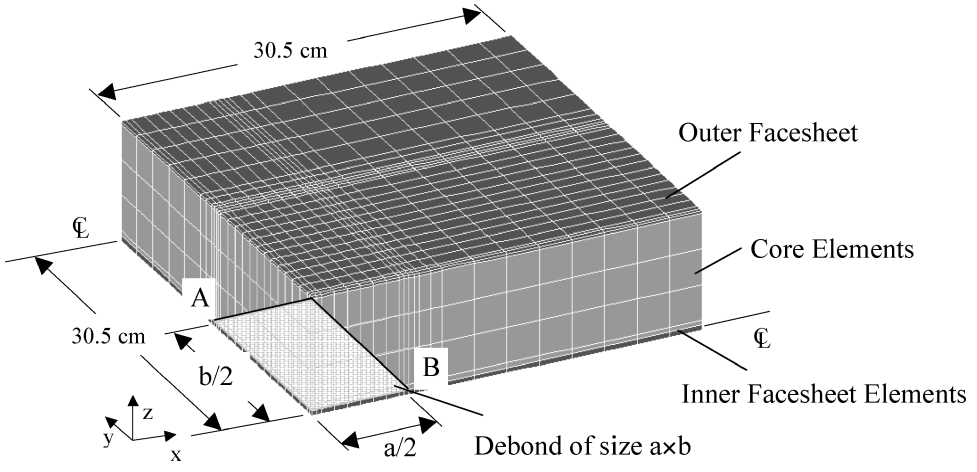

Fig. 7 Typical debonded sandwich model used in the analysis.

unit boundary conditions with constant displacements on the $x = 30.5$ cm and $y = 30.5$ cm planes but with net zero forces in the x and y directions, respectively. Boundary condition set III represents free-edge boundary conditions on the $x = 30.5$ cm and $y = 30.5$ cm planes. The three boundary condition sets represent three different levels of constraint on the problem and were used to determine the effect of external boundaries on the strain-energy release rate calculations.

In the three sets of boundary conditions (BC) that follow, u_0 and v_0 are uniform displacements along the $x = 30.5$ cm and $y = 30.5$ cm planes, respectively; $\bar{F}_x$ and $\bar{F}_y$ are integrated (net) forces in the x and y directions on the $x = 30.5$ cm and $y = 30.5$ cm planes, respectively; and N_x and N_y are individual nodal forces in the x and y directions on the $x = 30.5$ cm and $y = 30.5$ cm planes, respectively.

BC set I:

$$u(0, y, z) = 0; \qquad u(30.5, y, z) = 0; \qquad v(x, 0, z) = 0$$

$$v(x, 30.5, z) = 0; \qquad w(30.5, 30.5, 0) = 0$$

BC set II:

$$u(0, y, z) = 0; \qquad u(30.5, y, z) = u_0$$

$$v(x, 0, z) = 0; \qquad v(x, 30.5, z) = v_0$$

$$w(30.5, 30.5, 0) = 0$$

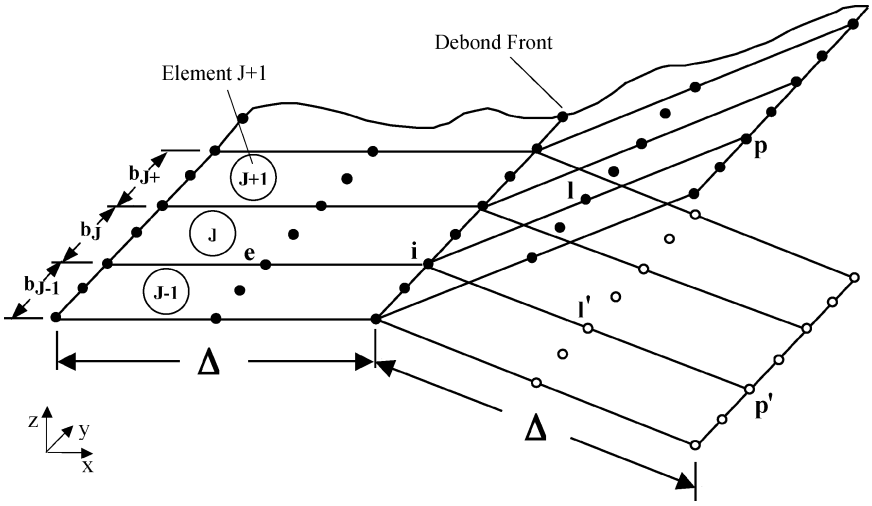

Fig. 8 Detail near the debond front and nodes in the strain-energy release rate calculations using VCCT.

and the net forces

$$\bar{F}_x(30.5, y, z) = 0; \qquad \bar{F}_y(x, 30.5, z) = 0$$

BC set III:

$$u(0, y, z) = 0; \qquad v(x, 0, z) = 0; \qquad w(30.5, 30.5, 0) = 0$$

and the forces

$$N_x(30.5, y, z) = 0; \qquad N_y(x, 30.5, z) = 0$$

Virtual Crack Closure Technique

The strain-energy release rates at stations A and B (see Fig. 7) along the debond front were calculated using the virtual crack closure technique (VCCT).[7,8] In the VCCT, the forces at and near the debond front are used in conjunction with the relative displacements behind the debond front. Figure 8 shows a typical portion of the finite element idealization near the debond front. The finite element mesh is made such that the element sizes ahead of and behind the debond front are identical and equal to Δ. Individual modes are calculated using

$$(G_{\mathrm{I}})_i = -(1/2\Delta b_{\mathrm{eq}})[F_{z_i}(w_p - w_{p'}) + F_{z_e}(w_l - w_{l'})]$$

$$(G_{\mathrm{II}})_i = -(1/2\Delta b_{\mathrm{eq}})[F_{x_i}(u_p - u_{p'}) + F_{x_e}(u_l - u_{l'})]$$

$$(G_{\mathrm{III}})_i = -(1/2\Delta b_{\mathrm{eq}})[F_{y_i}(v_p - v_{p'}) + F_{y_e}(v_l - v_{l'})] \qquad (3)$$

In Eq. (3), the b_{eq} is the equivalent width associated with nodes i and e and is obtained by following procedures similar to those used to determine constant load circulation as $(b_J + b_{J-1})/6$.

Fracture Mechanics Analysis Results

This section presents the fracture mechanics analysis results for various debond shapes and sizes. Rectangular debond configurations were considered as a basis for determining the effects of boundary conditions, panel curvature, debond size, and debond shape on strain-energy release rate values, for correlating with validation blowoff tests, and for approximating some of the foreign-object debris. Actual foreign-object debris configurations were also considered to determine specific strain-energy release rate values associated with the X-33 failure.

Rectangular Debonds

The strain-energy release rates were computed for the flat and curved sandwich-plate configurations shown in Table 6 and Fig. 6. The G_{I} values for the curved configurations are only slightly higher than those for the flat-plate configurations and differed by a maximum of about 8% for the largest debonds. This was an expected result, because this configuration (30.5 × 30.5 cm with radius of curvature of 122 cm) is nearly flat. Thus, only the curved-panel results are discussed and presented in Fig. 9. The G_{I} values at location B (see insert in Fig. 9) are presented as a function of dimension a, with fixed value of dimension b, for three pressures p of 276, 552, and 827 kPa. The analyses used to produce Fig. 9 were conducted before a final set of core internal pressures was determined; thus, the pressure values differ slightly from the values of 257, 464, and 786 kPa discussed earlier. As expected, the results suggest that G_{I} varies approximately with the square of the pressure and nearly linearly with debond size. Boundary condition sets I–III gave nearly identical values of G_{I}, suggesting negligible effects of the external boundaries on the strain-energy release rates for these configurations. For both the flat-plate and curved-plate models, the computed values of G_{II} were less than 10% of the computed G_{I} values. Thus, it was determined that the G_{I} values alone could be used as a metric of failure.

Blowoff Test

Blowoff tests were conducted to verify the finite element model. The two specimens for these tests were fabricated from 30.5 × 30.5 cm panels cut from undamaged material in lobe 1 of the LH_2 tank. The specimens were fabricated with a prescribed 2.54 × 6.67 cm rectangular debond between the core and inner facesheet and tested to failure with a uniform internal pressure loading (Fig. 10). The panel was pressurized through a pressure tap located directly under the fabricated debond.

The debond was fabricated by first removing a 2.54 × 6.67 cm section from the inner facesheet, then placing Teflon® tape over the exposed core and sharpening a short (less than 1 mm long) crack between the inner facesheet and core around the perimeter of the exposed core using a sharp hooked knife. In an attempt to make the cells in the honeycomb communicate and provide a uniform pressure distribution, the core of each panel was perforated by inserting a long thin needle through the wall of each of the cells. Fabrication of each specimen was completed with the reinsertion of the previously removed 2.54 × 6.67 cm section of inner facesheet and bonding of a tapered doubler patch. The 14.0 × 19.0 cm doubler patch was 0.05 cm thick with a 3.18-cm taper around its perimeter. Details of the blowoff test articles are found in Ref. 2.

The test panels were fabricated from the limited amount of undamaged material remaining in lobe 1. Because of the scarcity of available material, panel 1 contained a core splice, but panel 2 had a uniform core. The core splice in panel 1 (a location where adjacent honeycomb core sections are joined together with a foaming

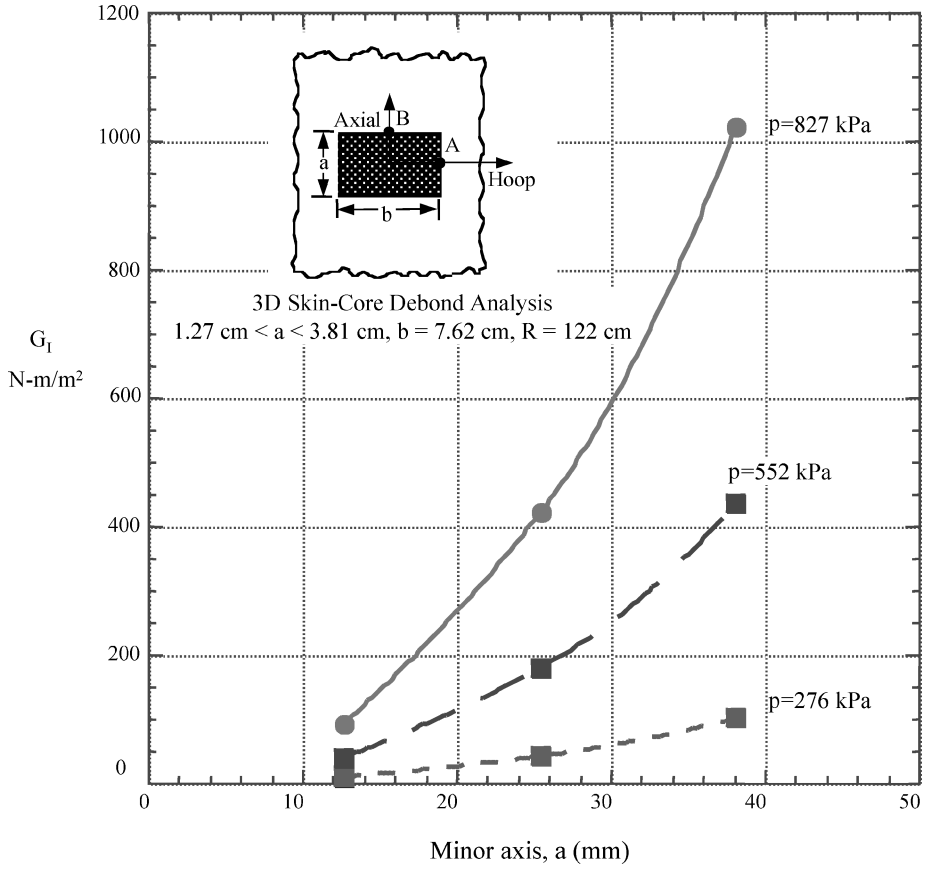

Fig. 9 Mode I strain-energy release rate for a rectangular debond in a curved sandwich panel.

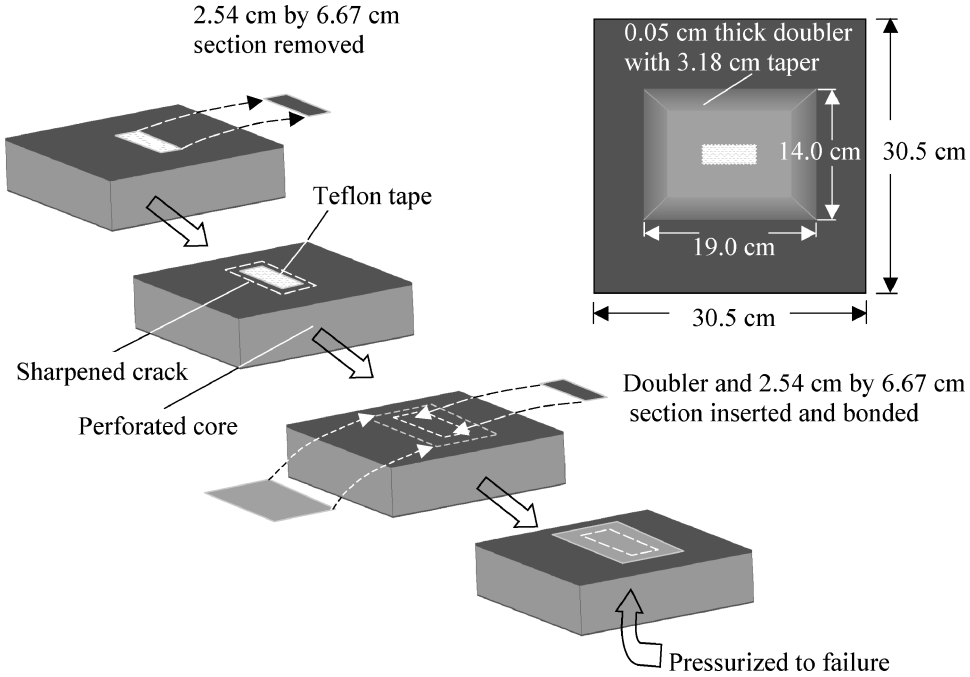

Fig. 10 Blowoff test specimens.

adhesive) was located beside one edge of the fabricated debond similar to the configuration shown in Fig. 5c. Single cantilever beam (see Appendix, Fig. A1b) and flatwise tensile test specimens were machined from a location adjacent to each of the test panels so that local values of strength and fracture toughness G_{cr} could be measured.

Figure 11 shows the fracture toughness values for the specimens used in the calibration of elastic moduli in the finite element models (SCB-Original Data), in the validation of the analyses (SCB-From Panels for Blow Off Tests), and from an alternate toughness test (Push-Off Tests).[9] The mean value and the 3σ upper and lower limit values (highest and lowest statistically possible values) were calculated for the fracture toughness determined from these specimens and are shown in the figure.

A finite element model was developed to represent the blowoff test panels. The core splice in panel 1 was not explicitly modeled

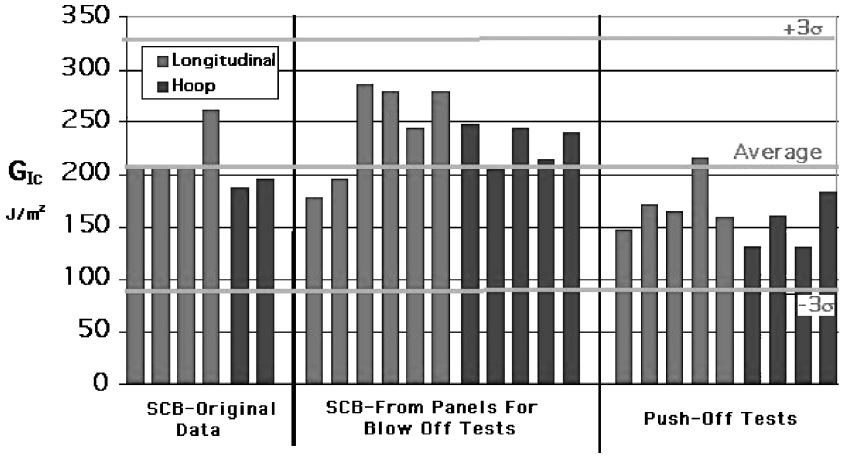

Fig. 11 Fracture toughness results from single cantilever beam test.

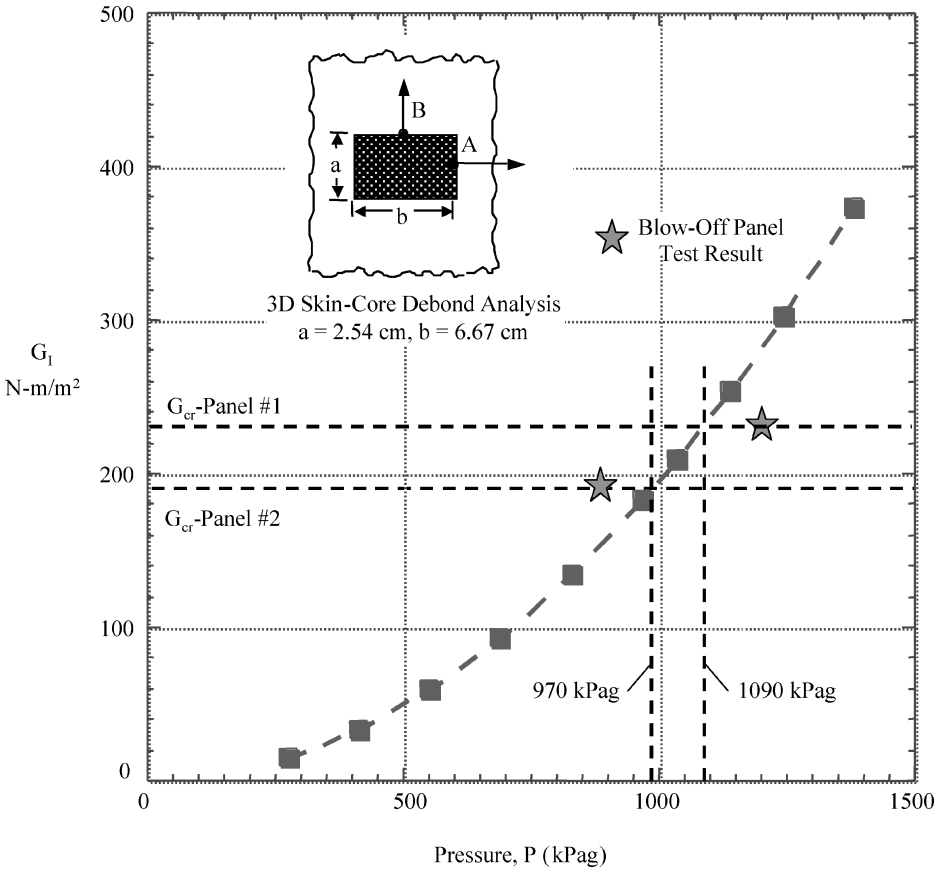

Fig. 12 Comparison of the predicted critical pressure for a 2.54 × 6.67 cm rectangular debond to the experimental results from the blowoff tests.

because the stiffness of the splice was not known; however, it was assumed that the debond would not grow through the splice because of the increased toughness caused by the foaming adhesive. The maximum predicted value of strain-energy release rate (located at point B) is plotted as a function of core pressure in Fig. 12. The dashed horizontal lines in the figure represent the mean values of the fracture toughness G_{cr} of each of the blowoff test panels. As noted earlier, the G_{cr} values were determined by single cantilever beam test specimens fabricated from material that was adjacent to the material used for each of the blowoff test panels (G_{cr}, panel 1, and G_{cr}, panel 2, in Fig. 12).

For panel 1, containing the core splice, the model predicted a failure pressure of 1090 kPag, while the actual failure pressure was measured as 1190 kPag. For panel 2, with the uniform core, the model predicted a failure pressure of 970 kPag while the actual failure pressure was measured as 880 kPag. In each case, the predicted failure pressure is the pressure corresponding to the intersection of the G_{cr} line for each panel and the G_I vs pressure curve, as shown in Fig. 12. Therefore, the difference in the predictions of failure pressure for panels 1 and 2 is caused by the difference in the mean value of fracture toughness determined by the single cantilever beam tests for each of the two panels.

The pressure transducers located throughout the core suggest that the pressure distribution in the blowoff test panels was not uniform. That is, a pressure gradient existed from the pressure transducer (located directly above the debond) to the specimen boundaries. To examine the effects of pressure distribution, the analyses were performed twice more, first with a uniform pressure distribution that

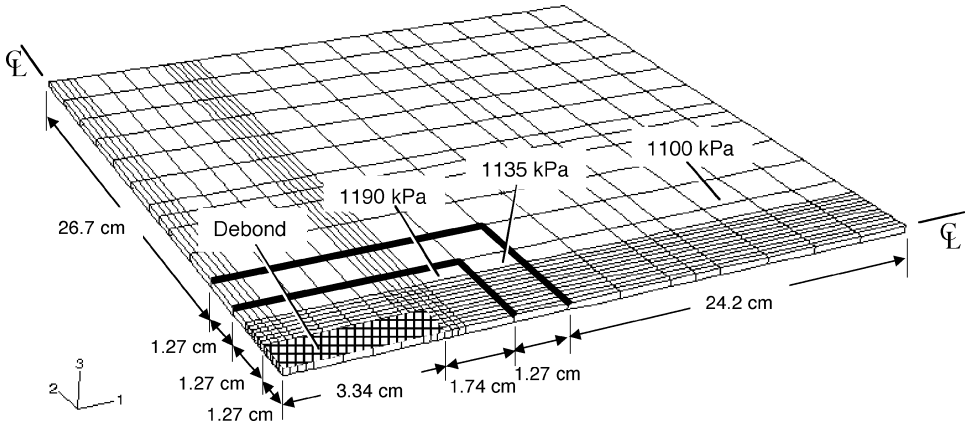

Fig. 13 Assumed pressure distribution in analysis of blowoff specimen 1.

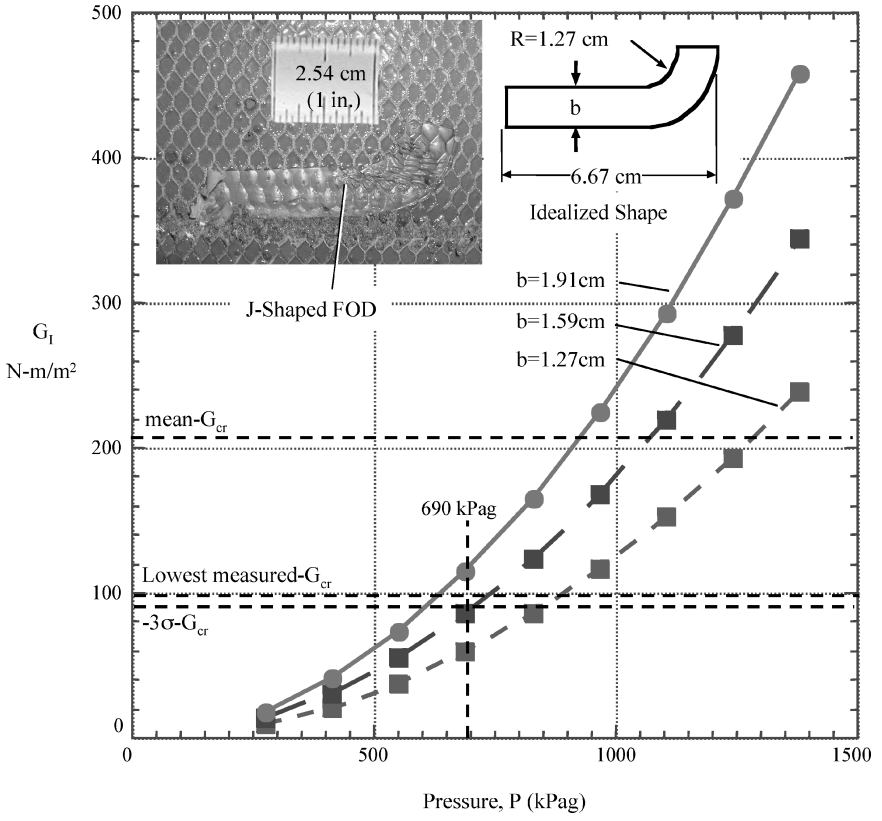

Fig. 14 Strain-energy release rates for a J-shaped FOD debond.

assumed that the maximum measured pressure at failure occurred throughout panel 1 (1190 kPag) and second with a pressure distribution corresponding to the measured pressure distribution at failure for panel 1. A representation of the measured pressure distribution is shown in Fig. 13 and varies from 1190 kPag at the debond to 1100 kPag along the specimen boundaries. The computational results showed that the strain-energy release rates computed in the two analyses differed by less than 3%, indicating that the local value of pressure at the debond governs G_{I}. Differences between the model predictions and the test results are within the numerical accuracy of the analysis method and within the scatter in the fracture toughness data. Thus, the finite element model and the fracture mechanics methods that were used in the remainder of the analyses are considered to be suitable for interrogating the several flaw configurations found in lobe 1 of the tank.

Several Known Flaw Configurations

Several flaw configurations were found in lobe 1 after the tank failure. These flaws included pieces of Teflon tape that might have originally been unsecured scrap from the bagging process used in assembly of the tank and unbonded regions where adhesive was omitted during the assembly process. Strain-energy release rates were computed for these initial flaw configurations using the verified analysis to determine whether debond growth would occur.

The local values of the internal core pressure and the core-to-inner facesheet bondline fracture toughness at the location of the initial flaws were not known. Additionally, the effective size of several of the initial flaws could not be determined because the FOD cut through cell wall boundaries. Thus, arguments based on the statistically possible values of pressure and fracture toughness and physically reasonable values of debond width are used in the discussion that follows. The mean value, lowest measured value, and the lowest statistically possible fracture toughness G_{cr}, as determined from the single cantilever beam test in Fig. 11, are shown as horizontal dashed lines in Figs. 14 and 15. Note that the lowest measured G_{cr} is only slightly higher than the $-3\sigma - G_{\mathrm{cr}}$ value.

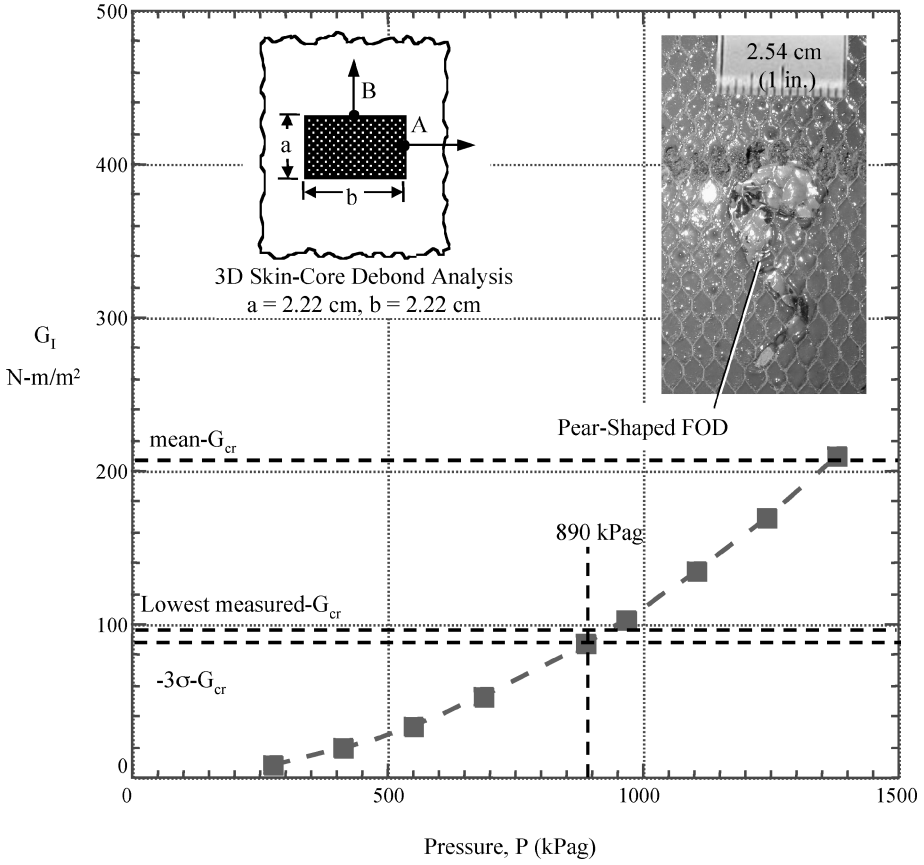

Fig. 15 Strain-energy release rates for a pear-shaped FOD debond.

J-Shaped Foreign-Object Debris Debond

A 1.27-cm-wide Teflon tape FOD and the corresponding idealized J-shape used in the finite element models are shown in the inserts of Fig. 14. Because the Teflon tape cut through cell wall boundaries, determination of the actual debond width was not possible. Therefore, three different values were considered to approximate the range of effective widths. The lower bound, upper bound, and most likely value of debond width b were determined to be about 1.27, 1.91, and 1.59 cm, respectively. The lower bound was considered to be the width of the Teflon tape (1.27 cm), whereas the upper bound was considered to be almost one cell width (0.48 cm) wider than the Teflon tape. The estimated upper bound was considered to be reasonable because of the very thin honeycomb cell walls as shown in the insert of Fig. 14. The most likely value was taken as the average of these two bounds.

The maximum value of mode I strain-energy release rate G_{I} is plotted as a function of internal core pressure in Fig. 14. Using the intersection of the lowest statistically possible value of fracture toughness $(-3\sigma - G_{\mathrm{cr}})$ line and the G_{I} vs pressure curve for a most likely value of debond width of 1.59 cm, the critical core pressure was determined to be 690 kPag. This value is less than the highest statistically possible (3σ) pressure in lobe 1 of the tank of 786 kPag. Therefore, it is believed that the J-shaped debond contributed to the tank failure.

Pear-Shaped Foreign-Object Debris Debond

The computational results for a pear-shaped Teflon tape FOD are presented in Fig. 15 using the format described earlier. The FOD, as shown in the insert in Fig. 15, was modeled as a 2.22×2.22-cm-square debond by assuming that the wide region of the FOD coalesced into a more uniform region. Using the intersection of the lowest statistically possible value of fracture toughness $(-3\sigma - G_{\mathrm{cr}})$ line and the G_{I} vs pressure curve, the critical core pressure was determined to be 890 kPag. This is greater than the highest statistically possible pressure in lobe 1 of the tank of 786 kPag. Therefore, it is unlikely that the pear-shaped debond contributed to the tank failure.

Unbonded Strip

Fracture mechanics analyses for a 0.127×61 cm unbonded strip (unbond) between the inner and outer facesheets at the lobe 1 to 4 longeron were also performed. This unbond is a manufacturing flaw caused by a gap in the adhesive used to join the core to the facesheets at the sandwich closeout. A photograph of the region near the unbond is shown in Fig. 16a, and the corresponding plane-strain finite element model is shown in Fig. 16b.

Three scenarios were considered. The first scenario was used to determine whether the unbond could have initiated the tank failure. Because the internal tank pressure during the proof test resulted in compressive local forces acting near this longeron, the unbond could not grow and therefore could not have initiated the tank failure. The second scenario was used to determine whether the unbond could have initiated the debond between the core and inner facesheet as a result of the high core pressures experienced just before the lobe failure. A 690-kPag core pressure with the core to inner facesheet bond intact resulted in a G_{I} of 2.45 $\mathrm{N \cdot m/m^2}$. The value of fracture toughness along the inner facesheet to outer facesheet bondline (approximately the toughness of the AF-191 adhesive) is about 1210 $\mathrm{N \cdot m/m^2}$ (Ref. 4), whereas the values for the facesheet to core bondline toughness are in the range of 100–300 $\mathrm{N \cdot m/m^2}$. Thus, it is likely that the core debonded from the inner facesheet before the unbond propagated between the facesheets. The third scenario was used to determine whether the inner facesheet would debond from the outer facesheet at the unbond after the core debonded from the inner facesheet. In this scenario, the maximum value of G_{I} was about 3820 $\mathrm{N \cdot m/m^2}$ for a 690-kPag core pressure, which is well above the fracture toughness of the adhesive (1210 $\mathrm{N \cdot m/m^2}$), and explains the continued debond growth along the lobe 1 to 4 longeron.

a) Photograph of unbonded 0.127 cm strip

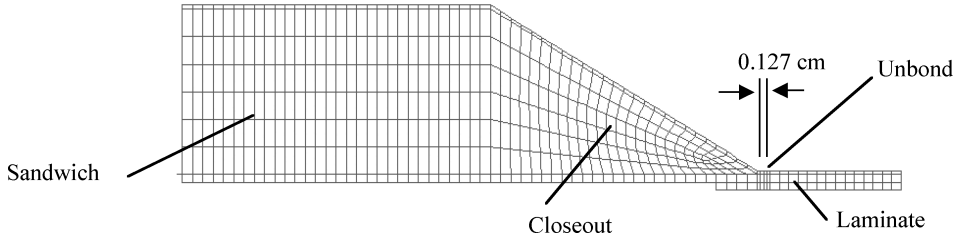

b) Finite element model used in fracture mechanics analysis

Fig. 16 Strain-energy release rates for the 0.127 × 5.08 cm unbond between upper and lower facesheet at the lobe 1 to 4 longeron.

Summary

This paper presented the failure analyses and testing conducted to determine the causes of the X-33 liquid-hydrogen tank failure. A ply-level stress analysis was conducted to explain the presence of microcracks in the plies of the inner and outer facesheet laminates. The stress analysis indicated that the ply-level transverse stresses caused by thermal residual effects and mechanical strains in the inner facesheet caused by internal pressure were greater than the transverse ply strengths and caused the microcracking. These microcracks allowed the infiltration of gaseous hydrogen that produced higher than expected sandwich core pressures in the X-33 liquid-hydrogen tank.

The posttest visual examination of the core-to-inner facesheet bondline revealed the presence of foreign-object debris. A long unbond between the inner and outer facesheets at the longeron between the tank lobes and a coalesced debond were also discovered. Fracture mechanics analyses based on finite element models of the debond configurations and the virtual crack closure technique were conducted to estimate the critical core pressure for unstable debond growth. The material properties in the finite element models were first calibrated with single cantilever beam tests. Once the analyses were calibrated, the effects of debond size, material properties, and magnitudes of the pressure loading on strain-energy release rates were determined. Computed strain-energy release rates were compared with experimentally determined values from two panel tests (blowoff tests) to validate the analyses and determine the conditions required for debond growth. The models predicted the failure pressure from the blowoff tests very well. Next, the fracture mechanics analyses for debonds caused by initial flaws were performed. The fracture mechanics analyses indicated that the combination of a higher than expected internal core pressure, a lower than expected bond-line toughness, and a debond initiated by a J-shape Teflon tape foreign-object debris are the likely causes of the failure of the X-33 LH_2 tank.

Appendix: Model Correlation to Experimental Results

The material properties in the models were calibrated by comparing finite element predictions for compliance, critical load, and toughness to their experimentally determined values. The experimentally determined values were obtained using the single cantilever beam (SCB) test shown in Fig. A1a. A detail of the SCB specimen showing the debond between the inner facesheet and core of the sandwich material is shown in Fig. A1b. The SCB test was performed by bonding the outer facesheet to a translational stage and applying a vertical load to the debonded end of the inner facesheet as shown in Fig. A1c. Figure A1c shows the quantities measured during this test (applied load P, debond length a, and opening displacement δ).

Values of compliance and strain-energy release rates computed from the finite element models are sensitive to the modulus of the facesheet laminates and core, and the reported values of material moduli vary significantly depending on the source. For instance, the reported value of facesheet transverse modulus at room temperature E_{22} differs by up to 20% depending on the source (Table 4). Because of uncertainty in the material property data, the more critical material properties (the facesheet bending moduli E^b_{11}, E^b_{22}; the core out-of-plane modulus E_{33}; and the core out-of-plane shear moduli G_{13} and G_{23}) for the model were calibrated so that numerical results from a plane-strain finite element model of the SCB test matched the corresponding measured values.

The calibration process for the finite element model is as follows: The material properties of the facesheets and core were adjusted so that the compliance of the sandwich structure in the longitudinal direction as determined by both the finite element model and the test matched for an intermediate debond length ($a = 51.4$ mm). The material properties were then verified by comparing compliance values over the entire range of interest (26.7 mm $\leq a \leq$ 72.4 mm). Then, the process was repeated by adjusting the properties of the facesheets and core so that the compliance in the hoop direction as determined by both the model and the test matched over the entire range of debond lengths.

The first property to be considered was the equivalent bending modulus of the inner facesheet in the longitudinal direction E^b_{11}. This property can be interpreted as the bending modulus E^b_{11} of a homogeneous material required to provide the same bending stiffness D_{ij} as the composite facesheet. For most laminates, this will be different from the extensional modulus E_{11} of the composite laminate and is a function of the ply stacking sequence. For example, if the stiffer plies in the laminate are grouped on the outside

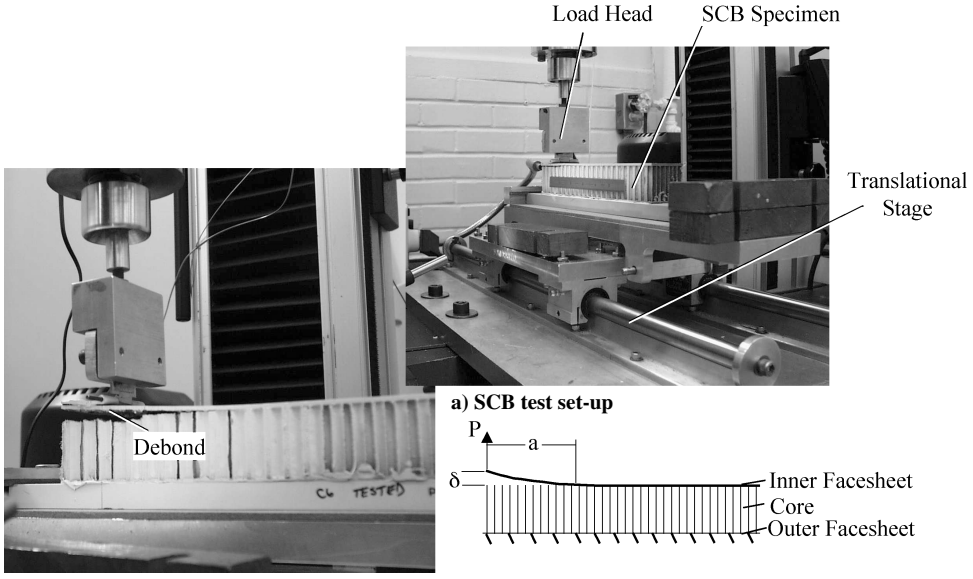

Fig. A1 Single cantilever beam test.

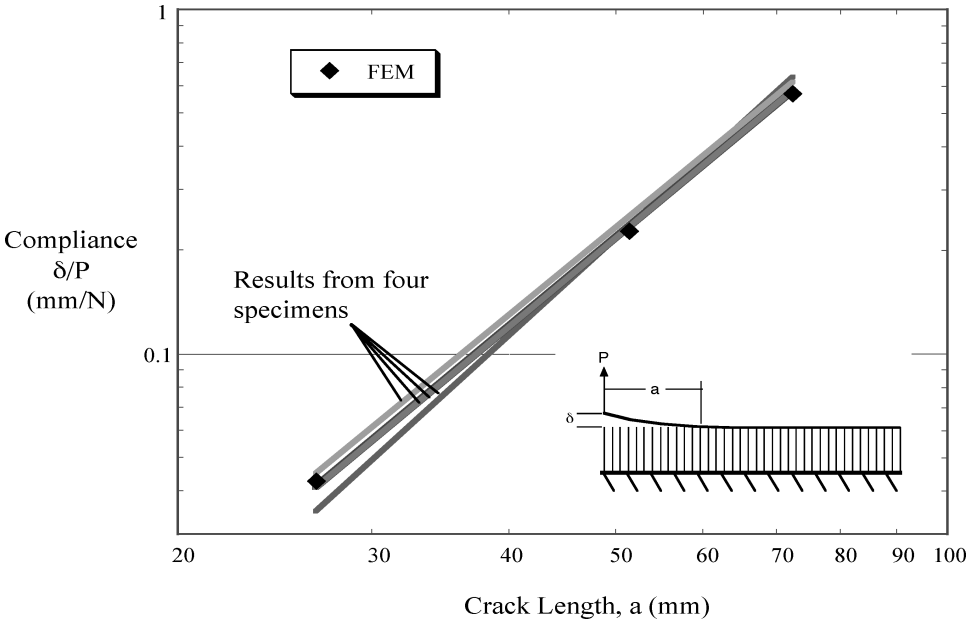

Fig. A2 Finite element method compliance correlation in longitudinal direction.

of the laminate the bending modulus will be higher than the extensional modulus. In the current case, the stiffer plies are grouped in the center, making the bending modulus lower than the extensional modulus.

Using classical lamination theory, the originally reported material properties, and a ply thickness of 0.0132 cm, the longitudinal bending modulus E_{11}^{b} of the inner facesheet was determined to be 15.5 GPa. However, using this value, the finite element model predicted higher deformations than those measured in the SCB tests, indicating that the original estimate of values for the longitudinal bending modulus of the inner facesheet was low. A value of longitudinal bending modulus of 19.3 GPa yielded values of compliance that were nearly equal to the measured values. Further, this value of bending modulus determined from a fit to the SCB data is only 2% lower than the 19.7 GPa value determined with a three-point bend test (performed at NASA Langley Research Center as part of the X-33 LH_2 tank-failure investigation) of the inner facesheet. Once the bending modulus was scaled to 19.3 GPa, the model and test gave similar compliance values over the range of crack lengths considered for four specimens as shown in Fig. A2.

Strain-energy release rates were determined by fitting a power law curve through the critical load P_c vs debond length a data for four specimens at each of the debond lengths considered (Fig. A3). This power law equation was then used to determine the input loads for the finite element model used to determine G_{IC}. Figure A4 shows excellent correlation between the G_{IC} vs a test data and finite element predictions over the entire range of debond lengths considered.

A similar strategy was used to correlate the finite element model to the SCB tests in the hoop direction. The first analyses were performed using a bending modulus in the hoop direction E_{22}^{b} of 100.7 GPa. This value was calculated using classical lamination theory and the original lamina properties. However, the finite element model predicted lower deformations than those measured in the SCB tests, indicating that the original estimate of the hoop bending modulus of the inner facesheet was also high. A value of 77.9 GPa for hoop bending modulus improved correlation with the

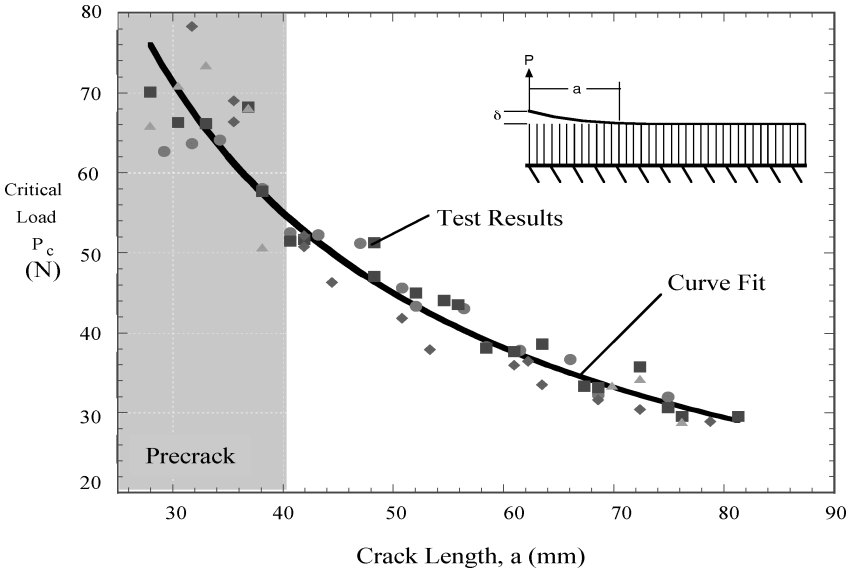

Fig. A3 Critical load determination in longitudinal direction.

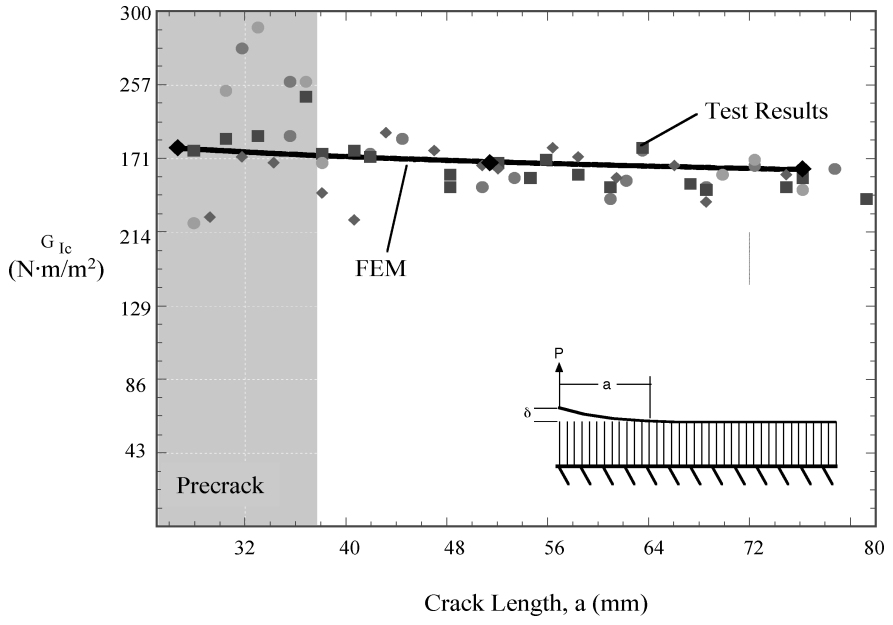

Fig. A4 Finite element method toughness correlation in longitudinal direction.

experimentally determined compliance at the intermediate debond length but did not account for some deviation at longer and shorter debond lengths. The bending modulus of 77.9 GPa used in the analyses is within about 10% of the 86.2-GPa modulus measured from a three-point bend test of an inner facesheet specimen oriented in the hoop direction (performed at NASA Langley Research Center as part of the X-33 LH_2 tank-failure investigation).

The core moduli (E_{33}, G_{13}, and G_{23}) were then adjusted to obtain agreement over the range of debond lengths. Although the fidelity of the original core properties was uncertain, it was found that the core properties of $E_{33} = 140$ MPa, $G_{13} = 74.5$ MPa, and $G_{23} = 15.9$ MPa fit the test results well. Here subscript 1 indicates the ribbon direction of the core or longitudinal direction of the tank, subscript 2 indicates the transverse or hoop direction, and subscript 3 indicates the out-of-plane direction.

Strain-energy release rate calculations from the finite element model again relied on the critical loads determined from the SCB tests. The procedure used to obtain a best-fit curve through the experimental data was similar to that described earlier for the longitudinal direction. Again, the strain-energy release rate values from the FEM model closely agreed with the measured values.

This process for correlating the plane-strain finite element model results to the corresponding experimental values provided a consistent set of stiffness properties to be used in the finite element model for predicting the strain-energy release rate for the various debonds found in lobe 1. A full list of properties used in the finite element model is shown in Table 5.

References

[1]Polland, D. R., Finn, S. R., Griess, K. H., Hafenrichter, J. L., Hanson, C. T., Ilcewicz, L. B., Metschan, S. L., Scholz, D. B., and Smith, P. J., "Global Cost and Weight Evaluation of Fuselage Side Panel Design Concepts," NASA CR 4730, April 1997.

[2]"Final Report of the X-33 Liquid Hydrogen Tank Test Investigation Team," NASA, May 2000.

[3]Henley, E. J., and Kumamoto, H., *Reliability Engineering and Risk Assessment*, Prentice–Hall, Upper Saddle River, NJ, 1981.

[4]Butkus, L. M., Mathern, P. D., and Johnson, W. S., "Tensile Properties and Plane-Stress Fracture Toughness of Thin Film Aerospace Adhesives," *Journal of Adhesion*, Vol. 66, No. 1–4, 1998, pp. 251–273.

[5]Raju, I. S., Shivakumar, K. N., and Crews, J. H., Jr., "Three-Dimensional Elastic Analysis of a Composite Double Cantilever Beam Specimen," *AIAA Journal*, Vol. 26, No. 12, 1988, pp. 1493–1498.

[6]*ABAQUS/Standard User's Manual*, Ver. 5.8, Hibbitt, Karlsson, and Sorensen, Inc., Pawtucket, RI, 1999.

[7]Rybicki, E. F., and Kanninen, M. F., "A Finite Element Calculation of Stress-Intensity Factors by a Modified Crack-Closure Integral," *Engineering Fracture Mechanics*, Vol. 9, No. 4, 1977, pp. 931–938.

[8]Raju, I. S., "Calculation of Strain-Energy Release Rates with Higher Order and Singular Finite Elements," *Engineering Fracture Mechanics*, Vol. 28, No. 3, 1987, pp. 251–274.

[9]Gates, T. S., and Herring, H. M., "Facesheet Push-Off Tests to Determine Composite Sandwich Toughness at Cryogenic Temperatures," *Proceedings of the AIAA/ASME/ASCE/AHS/ASC Structures, Structural Dynamics and Materials Conference*, Vol. 1, 2001, AIAA, Reston, VA, pp. 323–333.

T. Collins
Associate Editor